Dynamics of Atmospheres and Oceans 86 (2019) 116–133

Contents lists available at ScienceDirect

Dynamics of Atmospheres and Oceans

journal homepage: www.elsevier.com/locate/dynatmoce

Generation of oceanic internal gravity waves by a cyclonic surface stress disturbance

Georg S. Voelker[a,*], Paul G. Myers[b], Maren Walter[a], Bruce R. Sutherland[b,c]

[a] MARUM – Center for Marine Environmental Sciences, University of Bremen, Germany
[b] Department of Earth and Atmospheric Sciences, University of Alberta, Edmonton, Alberta, Canada
[c] Department of Physics, University of Alberta, Edmonton, Alberta, Canada

ARTICLE INFO

Keywords:
Internal gravity waves
Geostrophic adjustment
Air-sea coupling
Ocean modeling
Boussinesq approximation

ABSTRACT

Atmospheric cyclones with strong winds significantly impact ocean circulation, regional sea surface temperature, and deep water formation across the global oceans. Thus they are expected to play a key role in a variety of energy transport mechanisms. Even though wind-generated internal gravity waves are thought to contribute significantly to the energy balance of the deep ocean, their excitation mechanisms are only partly understood.

The present study investigates the generation of internal gravity waves during a geostrophic adjustment process in a Boussinesq model with axisymmetric geometry. The atmospheric disturbance is set by an idealized pulse of cyclonic wind stress with a Rankine vortex structure. Strength, radius and duration of the forcing are varied. The effect upon wave generation of stratification with variable mixed-layer depth is also examined.

Results indicate that internal gravity waves are generated after approximately one inertial period. The outward radial energy flux is dominated by waves having structure close to vertical mode-1 and with frequency close to the inertial frequency. Less energetic higher mode waves are observed to be generated close to the sea floor underneath the storm. The total radiated energy corresponds to approximately 0.02% of the wind input. Deeper mixed-layer conditions as well as weaker stratification reduce this fraction.

The low energy transfer rates suggest that other processes that drive vertical motion like surface heat fluxes, turbulent motion, mixed region collapse and storm translation are essential for significant energy extraction by internal gravity waves to occur.

1. Introduction

Storms play a major role in the global distribution of the wind work to the ocean (e.g. Price, 1983; Gill, 1984; Alford, 2001; Furuichi et al., 2008; Dippe et al., 2015) with the largest fraction of the transferred energy to the ocean leading to mixing and stirring of the surface boundary layer (Wunsch and Ferrari, 2004; Ferrari and Wunsch, 2009). A smaller part leads to the generation of near-inertial internal gravity waves that transfer this energy into the ocean interior (Leaman and Sanford, 1975; Leaman, 1976; Alford et al., 2012; Rimac et al., 2016). The generated waves eventually dissipate and thus potentially cause mixing at depth (Fu, 1981; Nagasawa et al., 2000; Alford and Whitmont, 2007; Danioux et al., 2008). Here we perform idealized simulations in order to gain insight into the mechanisms by which wind stress excites near-inertial gravity waves. Aiming at the characterization of the generation

* Corresponding author. Present address: Institute for Atmospheric and Environmental Sciences, Goethe University Frankfurt, Germany.
E-mail address: voelker@uni-bremen.de (G.S. Voelker).

https://doi.org/10.1016/j.dynatmoce.2019.03.005
Received 27 September 2018; Received in revised form 18 March 2019; Accepted 27 March 2019
Available online 29 March 2019

of internal gravity waves by the cyclonic wind structure we consider an axisymmetric wind stress and keep its translation equal to zero. By treating the wind stress disturbance stationary we isolate the effects of the rotational structure and the consequent generation of internal gravity waves independent of the advection by a vertically constant background flow equivalent to the translation of the cyclone. Simulations are performed that solve the fully non-linear, Boussinesq Navier–Stokes equations in an axisymmetric geometry. The action of the storm above the ocean is considered in a parameterization of the vertical momentum flux through the surface. Assuming the ocean is initially at rest, this setup is closely related to the axisymmetric spin up of a stratified fluid during early stages of the flow evolution (Duck and Foster, 2001; Moulin and Flór, 2004). At later times, the ocean evolution can be considered as a geostrophic adjustment process towards an equilibrated vortex. A theoretical analysis of the geostrophic adjustment process related to an axisymmetric vortex in the atmosphere was performed by Schubert et al. (1980). Simulations similar to the present approach but considering moving storms in a Cartesian geometry have been performed by Price (1983), Niwa and Hibiya (1997). Price (1983) focused on the description of the wake and the energetics of the flow which were compared to moored records. The wave–wave interaction in the wake was analyzed in detail by Niwa and Hibiya (1997). Bulatov and Vladimirov (2018) performed a more idealized study amenable to asymptotic analysis of internal waves generated by a translating point source.

Here we consider an ocean initially at rest and examine the spin up and the geostrophic adjustment due to a Rankine vortex type wind causing a bulk wind stress on the ocean surface. Rather than studying the energetics and structure of the wake of a moving storm (Price, 1983; Niwa and Hibiya, 1997), we focus on the excitation mechanisms of axisymmetric gravity waves of a non-translating disturbance. The detailed flow structure during and after a transient forcing as well as the energetics of the system are analyzed. Moreover, the linear and non-linear processes during the geostrophic adjustment are identified.

In Section 2 we introduce the model and its key parameters, derive analytic predictions for the model evolution and formulate an energy balance equation. The model results are presented in Section 3. The structure of the flow, the geostrophic adjustment of the ocean, the spectral structure of the radiated internal gravity waves and the energy balances are analyzed as the strength, radius, and duration of the forcing are varied. Additionally, we analyze how the energetics depend on the mixed-layer depth. Our results are summarized in Section 4.

2. Model description

2.1. Mathematical formulation

A non-linear, axisymmetric and Boussinesq model is used to simulate the ocean response to an axisymmetric wind stress acting on the surface (Fig. 1). The code is adapted from that used by McMillan and Sutherland (2010) and Holdsworth and Sutherland (2013). In particular, the axisymmetric Navier–Stokes equations are numerically solved for the perturbation density ρ, azimuthal vorticity $\zeta = \partial u/\partial z - \partial w/\partial r$ and the azimuthal velocity v. The governing equations are

$$\frac{\partial \zeta}{\partial t} = -\mathrm{ur}\frac{\partial}{\partial r}\left(\frac{\zeta}{r}\right) - w\frac{\partial \zeta}{\partial z} + \frac{1}{r}\frac{\partial}{\partial z}(v^2 + \mathrm{fvr}) + \frac{g}{\rho_0}\frac{\partial \rho}{\partial r} + D_1(\boldsymbol{\nu}, \zeta), \tag{1}$$

$$\frac{\partial v}{\partial t} = -u\frac{\partial v}{\partial r} - w\frac{\partial v}{\partial z} - \frac{1}{r}(\mathrm{uv} + \mathrm{fur}) + D_1(\boldsymbol{\nu}, v), \tag{2}$$

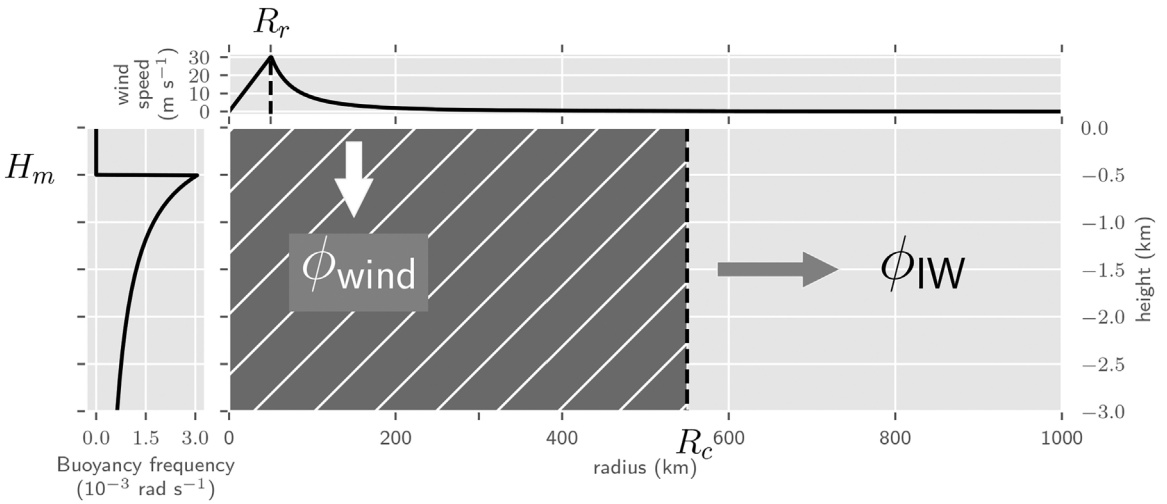

Fig. 1. Schematic of the model setup. A cyclone with a Rankine vortex structure prescribes the surface boundary conditions (upper panel). The stratification from Gill (1984) is used (left panel). The wind work ϕ_{wind} and the radiated energy flux ϕ_{IW} are estimated. R_r and R_c represent the radius of maximum wind forcing and the integration radius for the energy diagnostics, respectively. Their values, $R_r = 50$ km, and, $R_c = 550$ km, correspond to the values used in the control run. Here a mixed-layer depth, $H_m = 500$ m, is used for visualization.

$$\frac{\partial \rho}{\partial t} = -u\frac{\partial \rho}{\partial r} - w\frac{\partial \rho}{\partial z} - w\frac{\partial \bar{\rho}}{\partial z} + D_0(\boldsymbol{\kappa}, \rho), \tag{3}$$

in which u and w are the radial and vertical velocity, respectively, f is the constant Coriolis frequency, and g is the gravitational constant. The background and reference densities are denoted by $\bar{\rho}(z)$ and ρ_0. $D_n(\boldsymbol{\alpha}, X)$ is the dissipation operator with dissipation constant $\boldsymbol{\alpha} = (\alpha_r, \alpha_z)$ acting upon a field X. Explicitly,

$$D_n(\boldsymbol{\alpha}, X) = \alpha_r\left(\frac{1}{r}\frac{\partial}{\partial r}\left(r\frac{\partial X}{\partial r}\right) - \frac{n^2 X}{r^2}\right) + \alpha_z\frac{\partial^2 X}{\partial z^2}, \tag{4}$$

where n refers to the order of the Bessel function associated with the operator. The rate of diffusion of the azimuthal vorticity and velocity depend on the turbulent viscosity $\boldsymbol{\nu} = (\nu_r, \nu_z)$. Here we take $\nu_r = 10\,\mathrm{m}^2/\mathrm{s}$ and $\nu_z = 0.03\,\mathrm{m}^2/\mathrm{s}$. The kinematic viscosities are tuned so that the vortex formation and internal gravity wave radiation can be observed in reasonable computer simulation time while keeping the dissipation of the radiated internal gravity waves negligibly small. ν_z is many orders of magnitude larger than abyssal values but is taken to be representative of turbulent viscosity in the ocean below a storm. The turbulent diffusivity $\boldsymbol{\kappa} = (\kappa_r, \kappa_z)$ determines the effective diffusion of heat and salt through changes to the density perturbation. Given that the flow is turbulent, we assume $\boldsymbol{\nu} = \boldsymbol{\kappa}$. Corresponding to the horizontal and vertical scales L_h and L_z respectively are the diffusion time scales $T_h = {L_h}^2/\nu_h$ and $T_z = {L_z}^2/\nu_z$. For example, taking $L_z = 50$ m for the mixed-layer depth and taking $L_h = R_r = 50$ km for the radial scale of the forcing, the characteristic damping time scales are $T_h = 7.93$ years and $T_z = 0.96$ days. Here, R_r represents the radius of maximum forcing and thus the expected radial scales of the induced flow (cf. Fig. 1). The horizontal time scale being several orders of magnitude larger than the vertical time scale shows that vertical diffusion is dominant in this setup.

The stream function $\psi(r, z)$ is defined implicitly from the velocity field such that

$$u = -\frac{\partial \psi}{\partial z} \quad \text{and} \quad w = \frac{1}{r}\frac{\partial \psi}{\partial r}. \tag{5}$$

It is determined by inverting the vorticity equation

$$\Delta\psi - \frac{\psi}{r^2} = -\zeta \tag{6}$$

with $\Delta = r^{-1}\partial/\partial r(r\partial/\partial r) + \partial^2/\partial z^2$ being the scalar Laplacian operator in axisymmetric cylindrical coordinates.

The consideration of the azimuthal vorticity leads to a set of equations independent of the pressure p. Pressure itself is found from the diagnostic equation derived from the divergence of the radial and vertical velocity components of the momentum equations as well as the condition for incompressibility:

$$\frac{1}{\rho_0}\Delta p = -\left(\frac{\partial u}{\partial r}\right)^2 - \left(\frac{\partial w}{\partial z}\right)^2 - 2\frac{\partial w}{\partial r}\frac{\partial u}{\partial z} - 2\frac{u^2}{r^2} + \frac{1}{r}\frac{\partial}{\partial r}(v^2 + \mathrm{rfv}) - \frac{g}{\rho_0}\frac{\partial \rho}{\partial z} + \frac{1}{r}\frac{\partial}{\partial r}[rD_1(\boldsymbol{\nu}, u)] - \frac{\partial}{\partial z}D_0(\boldsymbol{\nu}, w) \tag{7}$$

The governing equations are discretized and solved on a staggered grid with a second-order finite-difference scheme. While the vertical coordinate spans the interval $-H = -3000\,\mathrm{m} \le z \le 0$ with a resolution of $\delta z = 23.44$ m, the radius is confined to the domain $0 \le r \le R = 1000$ km using a resolution of $\delta r = 976.56$ m. The prognostic equations are advanced with a leap-frog time-stepping scheme in which time-splitting errors are minimized by performing an Euler backstep at regular intervals (McMillan and Sutherland, 2010). The time step is equal to $\delta t = 18$ s.

Explicitly, Eqs. (6) and (7) are solved using a discrete Fourier sine transform in the vertical and a discrete Bessel transform in the radial direction. Given a function of radius $f(r)$ the Bessel transform is

$$F_n(k_j) = \sum_{m=0}^{n_z} r_m J_n(k_j r_m) f(r_m)\delta r. \tag{8}$$

Here, J_n denotes the Bessel function of the first kind of order n, $r_m = m\delta r$ and $k_j = \alpha_j/R$ where α_j is the jth zero of the Bessel function of order n. Hence $J_n(Rk_j) = 0$. The transform is computed for f between 1 and n_z. Inverting the vorticity equation (Eq. (6)) requires setting $n = 1$ whereas the pressure equation (Eq. (7)) is solved by setting $n = 0$. Differentiation of the stream function ψ yields the vertical and radial velocity according to Eq. (5). A fourth-order exponential wave number cutoff filter suppresses ringing in the transforms, as described in Appendix A.

2.2. Boundary conditions and background state

On the inner radial and bottom boundaries free-slip, no normal-flow conditions are imposed. Explicitly, this is done by setting $\psi = 0$ on the corresponding boundaries. A 10-point flow relaxation scheme at the outer radial boundary inhibits the reflection of internal waves back into the domain (Jensen, 1998). The radial wind stress τ_r and azimuthal wind stress τ_θ are coupled to the ocean surface velocities by the relation

$$\tau_r = \nu_z\rho_0\left(\frac{\partial u}{\partial z}\right)_{z=0} \qquad \tau_\theta = \nu_z\rho_0\left(\frac{\partial v}{\partial z}\right)_{z=0} \tag{9}$$

The wind stress is computed from the wind at 10 m height with the bulk formulation

$$\boldsymbol{\tau} = \rho_a C_{10} \boldsymbol{U}|\boldsymbol{U}|, \tag{10}$$

$$\boldsymbol{U} = \begin{pmatrix} u_{10} \\ v_{10} \end{pmatrix} - \begin{pmatrix} u \\ v \end{pmatrix}_{z=0}, \tag{11}$$

in which ρ_a is the density of air and the constant drag coefficient, C_{10}, is fixed at a value 10^{-3}. The stress then scales with the square of the velocity difference between the wind at 10 m height (u_{10}, v_{10}) and the surface velocity of the model ocean $(u, v)|_{z=0}$. For simplicity the radial wind component is zero at all times ($u_{10} \equiv 0$). Combined with the vertically discretized representation of Eq. (9), this yields a coupled system of equations for $(u, v)|_{z=0}$. It is solved analytically to obtain the wind stress and the surface velocity while maintaining a rigid-lid condition at the surface: $w|_{z=0} = 0$. The surface boundary condition for the azimuthal vorticity is therefore given by $\zeta|_{z=0} = \tau_r(\nu_z \rho_0)^{-1}$.

An idealized storm is simulated by imposing a time-dependent radial profile of azimuthal wind above the surface. For simplicity, a Rankine vortex is chosen so that the wind has a constant vertical vorticity within a radius R_r and zero vorticity beyond (Fig. 1). In particular, the wind magnitude increases linearly from zero at the origin to its maximum at R_r and beyond decreases with an inverse radial dependence. For a storm of duration ΔT_s the time evolution of the azimuthal wind, v_{10}, is set by linearly increasing its magnitude from zero to its maximum for quarter the storm duration, $\Delta T_s/4$, keeping it constant for $\Delta T_s/2$ and linearly decreasing its magnitude to zero for $\Delta T_s/4$. In the control run, the storm duration is set to $\Delta T_s = 48$ h, the radius to $R_r = 50$ km and the wind velocity to $v_{10} = 30\ \mathrm{m\,s^{-1}}$. Note that at zero wind conditions following the model storm there is a slight drag slowing down the surface currents. However, because the surface currents remain slow the effect is negligible and the wind stress is approximately zero. For comparison, a wind pulse with double the duration of ΔT_s is examined. The influence of the vortex radius, R_r, and the maximum value of the azimuthal wind, v_{10}, are also examined by doubling their value.

The background density profile $\bar{\rho}(z)$ is defined so that the buoyancy frequency, N, corresponds to the form used by Gill (1984):

$$N(z) = \begin{cases} 0, & \text{if } 0 > z > -H_m \\ \frac{s}{z_0 - z}, & \text{if } z \geq -H_m \end{cases} \tag{12}$$

with $s = N_0(z_0 - z_{ref})$. Here, H_m is the mixed-layer depth, which is set to 50 m in most simulations. Thus the buoyancy frequency is equal to N_0 at the reference height $z_{ref} = -H_m = -50$ m. We set the scaling height $z_0 = 150$ m and the depth of the domain to be $H = 3000$ m. Results are computed as they depend upon H_m as well as the maximum wind speed, v_{10}, the vortex radius, R_r, and the storm duration, ΔT_s. All model-related constants and reference parameters are summarized in Table 1.

2.3. A geostrophic adjustment process

In order to characterize the adjustment to a geostrophically balanced flow, we consider the linearized frictionless form of the

Table 1
Model setup related parameters. The radial wind profile has a Rankine vortex shape with critical radius R_r, where the wind is strongest. Wind speeds refer to the wind at 10 m height. The reference values for varying parameters are given in parenthesis.

Parameter	Value	Comment
Parameters fixed in all simulations		
ρ_0	$1027\ \mathrm{kg\,m^{-3}}$	Reference density of sea water
ρ_a	$1.2\ \mathrm{kg\,m^{-3}}$	Density of air
f	$10^{-4}\ \mathrm{rad\,s^{-1}}$	Coriolis frequency
N_0	$10^{-2}\ \mathrm{rad\,s^{-1}}$	Reference buoyancy frequency
ν_r	$10\ \mathrm{m^2\,s^{-1}}$	Radial kinematic viscosity
ν_z	$0.03\ \mathrm{m^2\,s^{-1}}$	Vertical kinematic viscosity
Pr	1	Prandtl number
C_{10}	10^{-3}	Drag coefficient
r_{max}	1000 km	Maximum radius
n_r	1024	Number of radial grid points
δr	976.56 m	Radial resolution
H	3000 m	Depth of domain
n_z	128	Number of vertical grid points
δz	23.44 m	Vertical resolution
t_{end}	40 days	Duration of simulations
δt	18 s	Time step
n_t	20	# of Time steps between Euler backsteps
R_c	550 km	Integration radius for energy diagnostics
Parameters varied in different simulations		
R_r	50–100 (50) km	Critical radius of Rankine vortex
$v_{10}(r = R_r)$	30–60 (30) $\mathrm{m\,s^{-1}}$	Maximum wind velocity
H_m	25–1000 (50) m	Mixed-layer depth
ΔT_s	48–96 (48) h	Storm duration

governing equations for small perturbations from the initially stationary basic state:

$$\frac{\partial u'}{\partial t} - \mathrm{fv}' = -\frac{1}{\rho_0}\frac{\partial p'}{\partial r} + \nu_z \frac{\partial^2 u'}{\partial z^2} \tag{13}$$

$$\frac{\partial v'}{\partial t} + \mathrm{fu}' = \nu_z \frac{\partial^2 v'}{\partial z^2} \tag{14}$$

$$\frac{\partial w'}{\partial t} + \frac{g\rho'}{\rho_0} = -\frac{1}{\rho_0}\frac{\partial p'}{\partial z} + \nu_z \frac{\partial^2 w'}{\partial z^2} \tag{15}$$

$$\frac{\partial \rho'}{\partial t} = w' \frac{\rho_0}{g} N^2 \tag{16}$$

$$0 = \frac{\partial w}{\partial z} + \frac{1}{r}\frac{\partial}{\partial r}(\mathrm{ru}'), \tag{17}$$

in which primes denote perturbed quantities. In this set of equations we neglect the horizontal diffusion terms as the vertical momentum diffusion is dominant in this setup. After some algebra and assuming $N^2(z) \neq 0$ the coupled linear equations are combined into a single equation:

$$\frac{\partial}{\partial t}\left[\frac{1}{r}\frac{\partial}{\partial r}(\mathrm{rv}') - \frac{\mathrm{f}}{\rho_0}\frac{\mathrm{g}}{}\frac{\partial}{\partial z}\left(\frac{\rho'}{N^2}\right)\right] = \frac{1}{r}\frac{\partial}{\partial r}\left(r\nu_z \frac{\partial^2 v'}{\partial z^2}\right). \tag{18}$$

Note that the first term on the left-hand side is the vertical component of the vorticity; the second term represents the spin-up by vortex stretching. Thus, in the absence of friction, Eq. (18) is a local potential vorticity conservation law. The final state at $t = \infty$ is characterized by $u_\infty = w_\infty = 0$ and

$$v_\infty = \frac{1}{f\rho_0}\frac{\partial p_\infty}{\partial r}, \qquad \rho_\infty = -\frac{1}{g}\frac{\partial p_\infty}{\partial z}, \tag{19}$$

in which the subscript ∞ denotes the stationary state as time approaches infinity. We differentiate (Eq. (18)) in radius and integrate in depth and time to get

$$\frac{\partial}{\partial r}\left[\frac{1}{r}\frac{\partial}{\partial r}(r\langle v_\infty\rangle)\right] + \frac{f^2}{H N^2}\frac{\partial v_\infty}{\partial z}\Bigg|_{z=-H}^{0} = \frac{1}{H}\frac{\partial}{\partial r}\left[\frac{1}{r}\frac{\partial}{\partial r}\left(r\int_0^\infty \mathrm{F}\,\mathrm{dt}\right)\right]. \tag{20}$$

Here, $\langle v_\infty\rangle$ denotes the depth-averaged terminal azimuthal velocity, H is the depth of the domain and $F(r, t) = \nu_z \partial v'/\partial z|_{z=0} = \tau_\theta/\rho_0$ is the wind forcing on the surface. Note that we have used the free-slip condition on the bottom on the right-hand side and Eq. (19) to reformulate the second term on the left-hand side. The initial state was assumed to be stationary. Due to a forcing in which there is negligible stress on the surface after a finite time and a free-slip condition at the bottom of the domain, we can assume zero friction at those boundaries, as $t \to \infty$. Consequently the second term on the left-hand side vanishes. The resulting equation is integrated in r to obtain

$$\langle v_\infty\rangle = \frac{1}{H}\int_0^\infty \mathrm{F}\,\mathrm{dt} + c(r) \tag{21}$$

The condition on the integration constant with respect to z, $c(r)$, is set so that $\partial/\partial r[r^{-1}\partial/\partial r(r\,c)]$ vanishes. This is true for any linear combination of functions proportional to r^{-1} and r. Requiring a bounded solution for zero and infinite radius leads to the conclusion that $c(r) \equiv 0$. Given a wind stress pulse resulting from the sudden manifestation of a Rankine vortex in the atmosphere and assuming the wind is much faster than the ocean surface velocity we have from Eq. (21)

$$\langle v_\infty\rangle = \frac{\rho_a C_{10} v_{10}^2 \Delta T_s}{6\rho_0 H}\begin{cases}\frac{r^2}{R_r{}^2}, & 0 < r \le R_r\\ \frac{R_r{}^2}{r^2}, & r > R_r\end{cases} \tag{22}$$

The above relation predicts the depth-averaged terminal azimuthal velocity with linear theory and horizontal internal stresses only. This analysis reveals some fundamental properties of the flow. Most importantly, with a rigid-lid approximation in place, the horizontal Reynolds stress, τ, is the only mechanism that initially transports momentum into the ocean interior. The structure of the terminal velocity is determined by the depth of the domain and the structure of the forcing only.

2.4. Energetics of the system

The energetics of the system are described in terms of the wind work Φ_{wind}, the energy radiated laterally by internal waves Φ_{IW}, the energy transferred to the vortex underlying the model storm E_v, and the dissipated energy D. Assuming an energetically isolated system, the energy balance is set up so that

$$\Phi_{\text{wind}} = E_{\text{v}} - \Phi_{\text{IW}} - D. \tag{23}$$

The wind work, the mechanical energy of the central vortex, as well as the radiated energy fluxes due to waves are calculated from the model results.

A general formula for the integrated wind power over a radius r and time interval of length ΔT, i.e. the wind work, is

$$\Phi_{\text{wind}}(r, \Delta T = T_2 - T_1) = \int_{T_1}^{T_2} \int_0^r \int_0^{2\pi} \boldsymbol{\tau}\cdot\boldsymbol{u}\, r'\, d\theta\, \text{dr}'\, \text{dt}, \tag{24}$$

in which $\boldsymbol{\tau}\cdot\boldsymbol{u}$ is the product of the wind stress and the ocean surface velocity. Given a forcing time $\Delta T_s = 2$ days and the characteristic scales of wind stress $\tau \sim 1\,\text{N/m}^2$, azimuthal velocity of the ocean in response to the wind stress $v \sim 0.1\,\text{m/s}$ and radial length scale $r \sim 50\,\text{km}$, the magnitude of the wind power can be estimated. It yields a value of the order $\Phi_{wind} \sim 100\,\text{TJ}$. Considering that this energy is imparted over a circle with a radius $r = 50\,\text{km}$ and a time span of 2 days, it is equivalent to the normalized wind work per area of the order $10^{-2}\,\text{MJ m}^{-2}$ and the average wind power per area of the order or $10^{-2}\,\text{W m}^{-2}$. This agrees well with observations of hurricanes (Sanford et al., 2011) and is one order of magnitude larger than modeled climatological energy fluxes in mid-latitude regions (Alford, 2001; Furuichi et al., 2008).

The energy associated with internal gravity waves leaving a cylinder with radius r in a time interval of length ΔT can be estimated using the average radial energy flux $\langle up\rangle$:

$$\Phi_{\text{IW}}(r, \Delta T) = \int_{T_2}^{T_1} \int_{-H_{\text{m}}}^{0} \int_0^{2\pi} \langle \text{up}\rangle\, r\, d\theta\, \text{dz}\, \text{dt}. \tag{25}$$

As a first order estimate of the radial energy transport we consider the propagation of a pulse of mode-1 internal gravity waves as described in Appendix B. In particular, for a frequency ω we have an average energy flux

$$\langle \text{up}\rangle = |A_u|^2 \frac{\rho_0(\omega^2 - f^2)}{2k_r\omega}\left(\frac{\partial}{\partial z}\hat{\psi}\right)^2 \frac{1}{k_r r} \tag{26}$$

in which A_u denotes the real amplitude of the radial velocity. In general A_u describes the amplitude as constant in time; however we consider a transiently excited quasi-monochromatic wave packet whose amplitude is non-zero for a time ΔT only. Integrating (Eq. (26)) over ΔT and over the cylinder with the radius r yields an expression for the total radiated energy:

$$\Phi_{\text{IW}} = |A_u|^2 \frac{\pi\rho_0(\omega^2 - f^2)}{k_r{}^2\omega}\Delta T \int_{-H}^{0} \left(\frac{\partial}{\partial z}\hat{\psi}\right)^2 \text{dz}. \tag{27}$$

For a rough estimate we take a typical amplitude of $|A_u| = 0.01\,\text{m/s}$, a radial wave number $k_r = \pi/R_{\text{r}}$, the time scales from the forcing, i.e. a frequency $\omega = 2\pi/12\,\text{h}^{-1}$ and $\Delta T = 2$ days, and assume a normalized vertical structure of the radial velocity so that $\int_{-H}^{0}\left(\frac{\partial}{\partial z}\hat{\psi}\right)\text{dz} = 1\,\text{m}$. The resulting prediction is then $\Phi_{\text{IW}} \sim 64\,\text{GJ}$ and thus corresponds to an approximate energy transfer of 0.06%. This estimate assumes that the primary mechanism transferring energy to internal gravity waves is the excitation of vertical mode-1 waves through forced motion in the stratified water column. In the previous section we concluded that the dominant forcing on the stratified region is the vertical momentum transfer through horizontal stresses. Buoyancy production through heat exchange between the ocean surface and the atmosphere as well as turbulent motion in the mixed region are strong drivers for vertical velocities (Bars et al., 2015; Lecoanet et al., 2015). Consequently, the sole consideration of wind induced surface stress, as employed in our model, may lead to small vertical velocities and little energy transfer to internal gravity waves.

The energy transferred to the central vortex is obtained by integrating the mechanical energy density within a cylinder of radius R_c enclosing the vortex.

$$E_{\text{v}}(t) = \int_{-H}^{0} \int_0^r \int_0^{2\pi} (\mathcal{E}_{\text{KE}} + \mathcal{E}_{\text{APE}}) r'\, d\theta\, \text{dr}'\, \text{dz} \tag{28}$$

This is done at a late time t so that excited internal gravity waves are radiated away and the result isolates the energy of the vortex. Note that the mechanical energy density is expanded in kinetic and available potential energy density. The former is given by

$$\mathcal{E}_{\text{KE}} = \frac{\rho}{2}(u^2 + v^2 + w^2). \tag{29}$$

The latter is estimated using the relation (Kang and Fringer, 2010)

$$\mathcal{E}_{\text{APE}} = \frac{g^2\rho^2}{2\rho_0 N^2} + \frac{g^3\rho^3}{6\rho_0^2 N^6}\frac{\partial}{\partial z}(N^2). \tag{30}$$

A prediction for the energy stored in the geostrophic vortex at late times can be obtained by using the late-time azimuthal velocity $\langle v_\infty\rangle$ (Eq. (22)), spatially integrated so that

$$E_v = \int_{-H}^{0} \int_0^{2\pi} \int_0^{\infty} \frac{\rho_0}{2}\langle v_\infty\rangle^2 r\, \text{dr}\, d\theta\, \text{dz} = \frac{\pi}{6\rho_0 H}\left(\frac{2}{3}\rho_{\text{a}} C_{10} v_{10}^2 \Delta T_{\text{s}} R_{\text{r}}\right)^2. \tag{31}$$

Evaluating Eq. (31) leads to an estimate of approximately $E_{\text{v}} \sim 1\,\text{TJ}$.

In summary, we predict an energy transfer from the wind input to internal gravity waves and a geostrophically balanced vortex of the order 0.01% and 1% relative to the wind work, respectively. This leads to a predicted dissipation of up to 99% of the wind work.

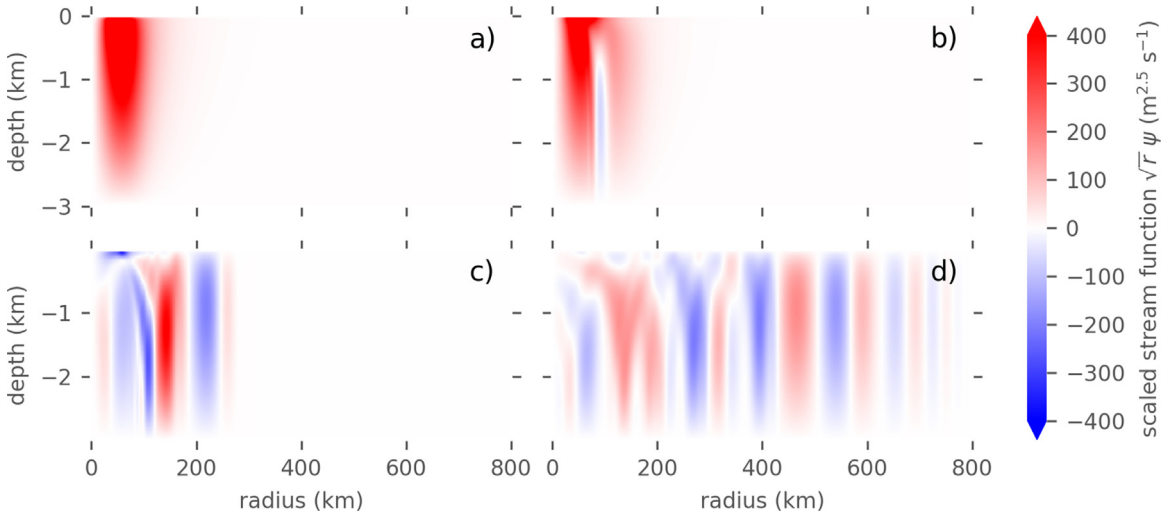

Fig. 2. Snapshots of scaled stream function for the control run at model time (a) 12 h, (b) 22.5 h, (c) 50 h and (d) 135.5 h. The last time is approximately ten inertial periods after the end of the forcing at 48 h. For scaling reasons the stream function was multiplied by the square root of the radius. This corresponds to the asymptotic behavior of the Bessel function of first kind for large radii.

For this estimate we neglected surface heat fluxes, heat induced convection, vertical turbulent motion and consequent mixing such that the vertical energy transfer is based on the vertical momentum flux only.

3. Results and discussion

3.1. Description of the control run

All simulations performed show qualitatively the same wave and vortex generation mechanisms. These are discussed here with regard to a control run in which the mixed-layer depth is $H_m = 50$ m and the critical radius of the Rankine vortex radial wind profile is $R_r = 50$ km. The associated maximal wind speed at 10 m height is $v_{10} = 30$ m/s. The time evolution of the wind is set by linearly increasing its magnitude from zero to its maximum for quarter the storm duration $\Delta T_s/4$, keeping it constant for $\Delta T_s/2$ and linearly decreasing its magnitude to zero over another $\Delta T_s/4$. In the control run, the storm duration is set to $\Delta T_s = 48$ h. For the qualitative visualization of the flow we use the scaled stream function, $r^{\frac{1}{2}}\psi$, with ψ as defined in Eq. (5). The scaling with the inverse square root of the radius is chosen to compensate the decreasing amplitude of the radiating gravity waves as they propagate radially outward.

During the first phase of the forcing the azimuthal surface velocity is accelerated due to the surface stress of the growing model storm. Consequently, the centripetal and the Coriolis force accelerate the fluid radially outward and drive an overturning motion with a maximum stream function near the Rankine radius, R_r (Fig. 2a). Upwelling and downwelling are induced respectively at radii smaller and larger than R_r. This motion forms immediately after the stress starts acting on the surface and leads to velocities with amplitudes up to 3 m/s within 12 h. The forced overturning leads to a density anomaly which in turn causes a bottom-intensified

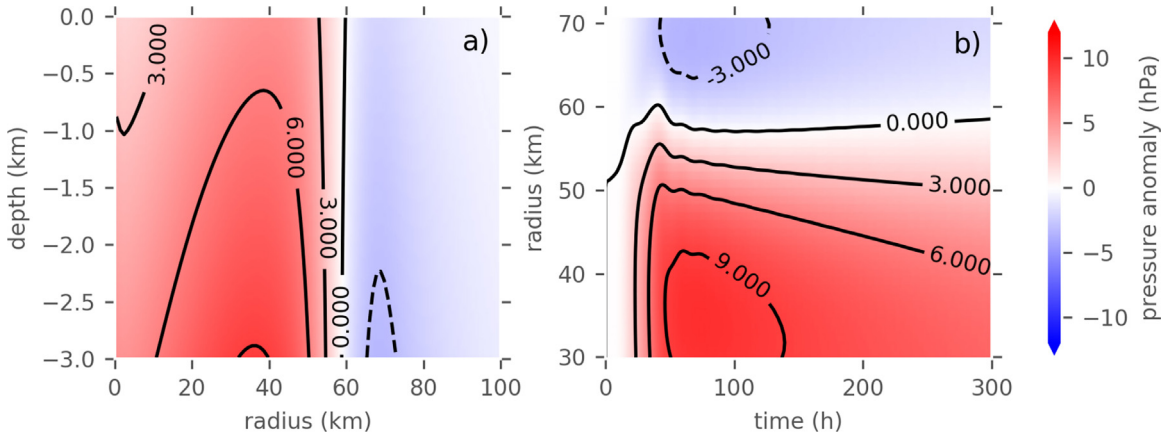

Fig. 3. (a) Snapshot of the pressure anomaly in the control run at time $t = 48$ h and (b) corresponding time evolution of the pressure anomaly on the bottom close to the radius of the Rankine vortex $R_r = 50$ km. Note that the magnitude of the pressure anomaly increases with depth.

positive pressure anomaly at radii smaller than R_r and a negative pressure anomaly at larger radii (Fig. 3a). During the constant phase (Fig. 2b) and the decrease of the wind stress forcing the Coriolis effect starts to counteract the described motion. The inertial oscillations reverse the flow and cause vertical motion with largest amplitudes close to R_r. The vertical motion extends throughout the whole water column including the stratified region below the mixed-layer depth. This inertial pumping corresponds to the generation mechanism for internal gravity waves suggested in the previous section. Induced dominant mode-1 internal gravity waves are observed to emanate radially away from the storm region (Fig 2 c). A second generation mechanism arises from the bottom pressure anomaly close to R_r. Being forced by the return flow of the surface inertial oscillation it oscillates with the Coriolis frequency and generates upward propagating internal gravity waves with higher vertical mode numbers (Figs. 2d and 3b).

The inertial period corresponding to the inertial frequency $f = 10^{-4}\,\mathrm{rad\,s^{-1}}$ is approximately 0.73 days. In comparison, the duration of the pulse is $\Delta T_s = 2$ days. However, the ramp-up and ramp-down phases, each of which is 0.5 days, correspond to linear changes in the wind and thus, quadratic changes in the wind stress amplitude. The effective forcing time is approximately twice the inertial period. Thus, the near inertial oscillations are most strongly excited.

3.1.1. Geostrophic adjustment of the vortex

The observed geostrophic adjustment occurs in three different phases. The first phase is the development of a geostrophically unbalanced azimuthal vortex while the wind stress acts on the surface. During this phase the surface and consequently the subsurface layers are accelerated in the azimuthal direction. The centripetal acceleration acts in a radially outward direction and consequently accelerates the radial and vertical velocity according to the (incompressible) continuity equation so that an overturning flow is excited (Fig. 2a). The forced horizontal and vertical velocities cause a change in the density anomaly profile as water with higher and lower density is heaved and pumped down at radii smaller and larger than R_r, respectively. Consequently a bottom-intensified pressure anomaly, as described above, develops.

The second phase is characterized by the inertial pumping, the advection of the azimuthal velocity through the mixed layer and the generation of internal gravity waves. This phase starts after one inertial period and quickly ends after ramping down the surface forcing as the inertial oscillation damps out. It therefore acts on a time scale of two inertial periods which is comparable to the duration of the forcing. A detailed description of the generation and propagation of internal gravity waves can be found in Section 3.1.

Overlapping the second adjustment phase, the decay of the mechanical energy of the vortex towards the geostrophic balance starts right after the end of the forcing (at time $t = 48$ h). This decay can be related to two separate processes. The first is the diffusion of the radially equilibrated azimuthal vortex in depth. The second is the adjustment of the bottom-intensified pressure structure. The radial gradient of the pressure anomaly accelerates the radial velocity outward and thus decelerates the azimuthal velocity through the Coriolis force throughout the whole water column. This deceleration is aligned with the diffusion process in the upper water column and counteracting it in the lower water column. Consequently the time scale for the adjustment is larger or smaller than the diffusion timescale when the vortex is shallow or deep, respectively. Comparing the energy decay in the control run to the evolution of the analytic solution to the diffusion problem with given initial conditions from the simulation shows that the observed time scale is approximately four times larger than the diffusion time scale.

In summary, there are three overlapping stages of adjustment in the simulations, each with a distinct time scale. The first is the spin-up of the vortex with the forcing time scale. In the second stage, the inertial oscillation decays until it reaches a horizontal geostrophic balance within less than ten inertial periods. This process is associated with the radiation of internal gravity waves. At the end the vortex diffuses in the vertical until a vertically uniform vortex is established. At the same time the adjustment of the bottom-intensified pressure dipole decelerates the central vortex. Depending on the vertical extent of the excited azimuthal vortex at the end of the forcing the timescale of this adjustment phase can be longer or shorter than the given vertical diffusion time scale. A quantitative analysis of the time scale of the last phase is done in Section 3.2.2.

3.1.2. Generation and propagation of waves

Whereas at radii close to the Rankine vortex radius, R_r, the inertial oscillation dominates the flow, it is characterized by radially outward propagating internal gravity wave packets with distinct radial group velocities in the far field (Fig. 2c and d). These are generated by two different mechanisms. The first and more dominant is the generation by inertial pumping. The inertial oscillation associated with the spin-up of the vortex beneath the wind forcing induce a return flow in the interior and a corresponding upwelling and downwelling at radii smaller and larger than the radius of the vortex, R_r. This vertical oscillation stretches throughout all the water column and induces near-inertial vertical mode-1 internal gravity waves. The second generation mechanism is related to a bottom-intensified pressure anomaly associated to the spin-up of the vortex (Fig. 3a). It oscillates with the inertial oscillation and locally generates upward propagating internal gravity waves with higher vertical mode structure (Fig. 2d and 3 b). Both generation mechanisms are associated to the second adjustment phase described above. The wave packets have distinct group velocities in the far field where higher vertical mode wave packets have lower radial group velocity. Depicting the maximal value in depth of the radial energy flux the wave packets appear as beams (Fig. 4). The visible group velocities can be described using the analytic solution of the vertical mode decomposition. In particular, the radial group velocity, c_g, is given by

$$c_g = k_r \frac{s^2}{{q_s}^2}\left(\frac{s^2 {k_r}^2}{{q_s}^2} + f^2\right)^{-\frac{1}{2}}, \tag{32}$$

where k_r is the radial wave number, q_s is the discrete vertical wave number obeying the discretization criterion (Eq. (B.8)) and

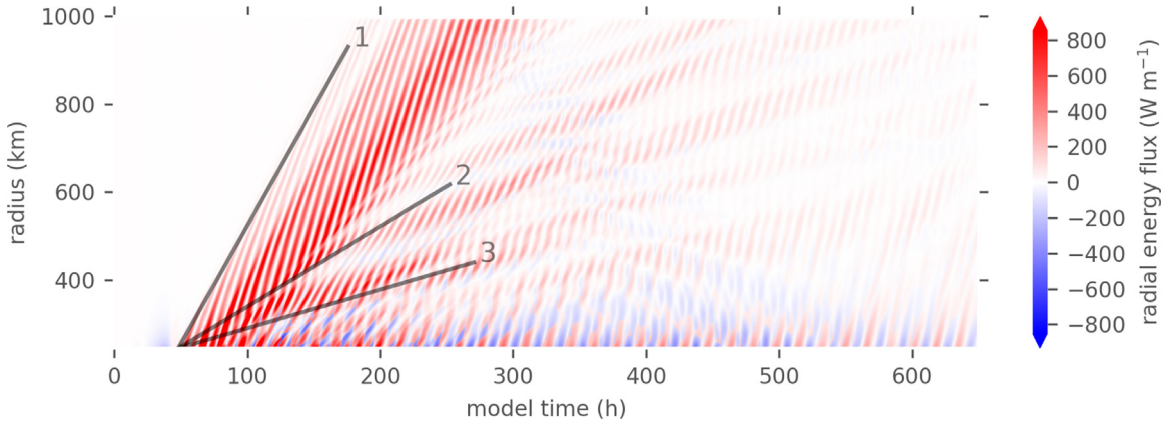

Fig. 4. Radial time series plot of the azimuthally integrated radial energy flux $\int_0^{2\pi} \phi_{\mathrm{IW}}\, r\, d\theta$ as a function of time and radius for control ($H_\mathrm{m} = 50$ m) run with the reference parameters listed in Table 1. The maximal value in depth is shown. The characteristic beams are wave packets with distinct vertical modes and group velocities which correspond to the group velocities predicted by the vertical mode decomposition (black overlay). A radial wave number $k_r = \pi/R_\mathrm{r}$ is assumed; mode numbers are indicated.

$s = N_0(z_0 + H_\mathrm{m})$, where N_0 is the maximum value of the buoyancy frequency profile (Eq. (12)). A detailed derivation can be found in Appendix B. For estimating the group velocities in Fig. 4 the radial wave number is set to $k_r = \pi/R_\mathrm{r}$ corresponding to twice the radius of the Rankine vortex while q_s corresponds to the first three positive solutions of the discretization equation (Eq. (B.8)). Note that higher vertical modes are generated not only in the forcing region but are also separating from the lower mode wave packet (Fig. (4)). They may be generated through non-linear wave–wave interactions within the packet.

The spectral structure of the induced internal gravity waves is analyzed in terms of the radial wave number-frequency spectrum for the vertical velocity at the mixed-layer depth, $z = -H_\mathrm{m}$, (Fig. 5a). Note that the cylindrical symmetry of the radiating waves requires a Fourier–Bessel transform (Eq. (8)) in the radial direction. The spectrum is characterized by distinct lines with largest amplitudes close to the inertial frequency. The structure of these lines resembles the dispersion relation (Eq. (B.10)) associated with vertical normal modes in the present stratification (Fig. 5b). The analytical dispersion relation overestimates the frequency of the spectrum as the scaled radial wave number $k_r R_\mathrm{r}$ approaches the cut off wave number at $k_r R_\mathrm{r}/2\pi = 5$ (cf. Appendix A). This effect might be associated to numerical attenuation. High spectral densities at low wave numbers and frequencies equal to f correspond to the inertial oscillation of the vortex.

3.2. Parameter dependencies of the flow structure

Here we present a qualitative analysis of the flow structure depending on the varied parameters with respect to the control run.

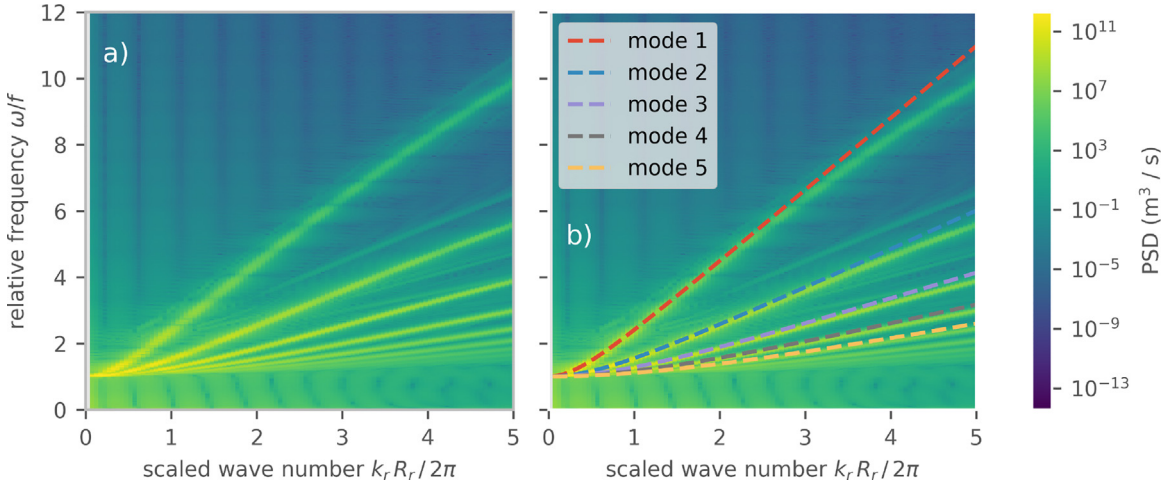

Fig. 5. (a) Wave number-frequency spectrum of the vertical velocity (scaled as power spectral density, PSD) from the control run at the mixed-layer depth. In accordance with the symmetry, a Fourier-Bessel transform was used in radial direction (Eq. (8)). The vertical velocity was multiplied with a 2-dimensional Hanning window to avoid ringing in the spectrum. (b) Like (a) with overlaid analytic dispersion relation for the first five vertical normal modes (Eq. (B.10)). The x-axes were limited to the radial cut off wave number to account for numerical attenuation (cf. Appendix A).

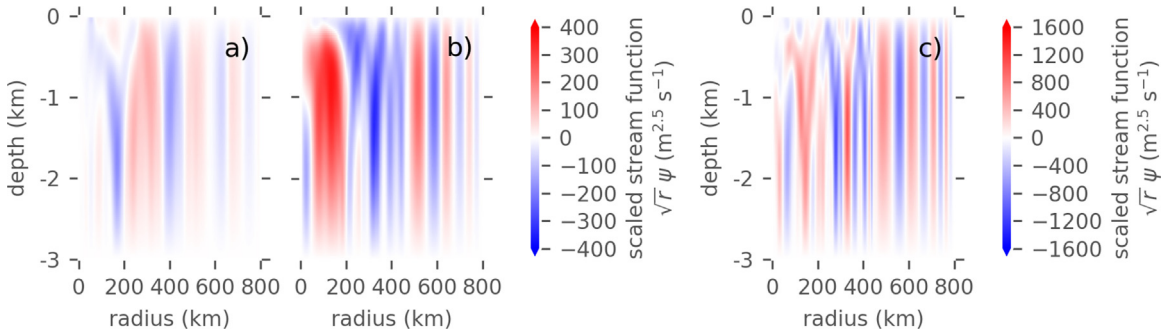

Fig. 6. Snapshots of the stream function 10 inertial periods after the forcing stops for different surface forcing parameters. The stream function is scaled with the square root of the radius to account for the decay of the internal wave amplitude with radius. The varied parameters are (a) $\Delta T_s = 96$ h, (b) $R_r = 100$ km and (c) $v_{10} = 60$ m s^{-1}. A separate color scale was set for (c) to account for the approximately 4 times larger velocities associated to two times stronger winds.

For visualization we show the stream function of the model runs 10 inertial periods after the end of the forcing (Figs. 6 and 7).

3.2.1. Surface forcing parameters

For the evaluation of the effect of the surface forcing parameters on the flow structure, three runs with twice the value of one of the parameters were performed. In particular, the duration of the wind forcing, ΔT_s, the radius of the Rankine vortex, R_r, and the maximum wind speed, v_{10}, were varied.

In the first experiment the duration of the forcing in all phases was doubled so that $\Delta T_s = 96$ h. The longer pulse acts over a time of approximately 3.5 inertial periods. Therefore, the wind stress is effectively out of phase with the inertial oscillation at the end of the pulse. It is observed that the wind forcing counteracts the inertial oscillation of the formed vortex, and therefore reduces the radial and vertical velocities. The amplitude of the inertial oscillation and radiated internal gravity waves is visibly smaller compared to the control run (Figs. 2d and 6a). Correspondingly, the radiation of columnar internal gravity waves is less pronounced. Thus the time scales of the wind pulse are important to the wave generation mechanism.

Doubling the Rankine vortex radius with respect to the control run, i.e. $R_r = 100$ km, influences the flow structure close to the azimuthal vortex but leaves the radiated internal gravity waves approximately unchanged. In particular, the linear increase of the wind at radii smaller than R_r and the inverse drop beyond R_r of the wind profile lead to an increase in amplitude by about 40% and

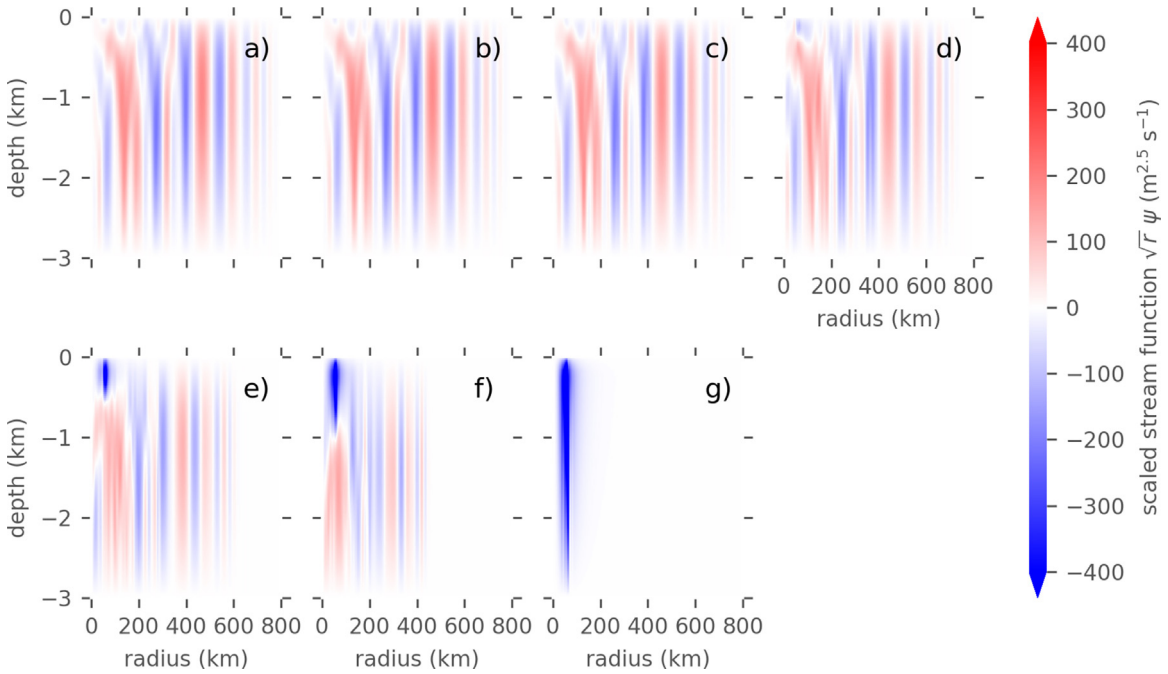

Fig. 7. Same as Fig. 6 but with varied mixed-layer depths. The stream function is scaled with the square root of the radius to account for the decay of the internal wave amplitude with radius. The mixed-layer depths are (a) $H_m = 25$ m, (b) $H_m = 50$ m (control run), (c) $H_m = 100$ m, (d) $H_m = 200$ m, (e) $H_m = 500$ m, (f) $H_m = 1000$ m and (g) $H_m = H = 3000$ m.

Table 2
Table of relative damping time scales of the kinetic energy within a radius $r \approx 250$ km. The effective damping time scales were found using a least squares fit of the analytic solution of the diffusion problem to the data. It was then compared to the solution with a diffusion time scale given by the model viscosity $T_z = {L_z}^2/\nu_z$. The last three rows refer to the simulations with double wind pulse duration, ΔT_s, double radius of the storm, R_r, and double wind speed, v_{10}.

H_m (m)	T_z^{eff}/T_z
25	4.41
50 (control run)	4.11
100	3.16
200	1.82
500	0.72
1000	0.33
3000	0.13
$\Delta T_s = 96$ h	5.17
$R_r = 100$ km	5.56
$v_{10} = 60\ m\ s^{-1}$	6.52

the radial length scales of the flow close to R_r are visibly larger (Fig. 6b). The radiated waves shift radially outward with the generation region equal to 50 km (Fig. 6b). However, the group velocities and wavelengths of the radiated waves do not change. Thus the radial length scale of the gravity waves is set by the forcing frequency and the dispersion relation (Eq. (32)) rather than the length scale of the forcing. It is approximately 100 km which corresponds to twice the Rankine vortex radius of the control experiment, even if it is not related to that parameter.

An increase of the wind speed by a factor 2 so that $v_{10} = 60\ m\ s^{-1}$ changes neither the structure of the generated vortex nor the properties of the radiated internal gravity waves with respect to the control run (Fig. 6c). The amplitude, however, changes by a factor 4, which is related to the square dependency of the wind stress on the wind speed (Eq. (10)).

To evaluate the effect of the surface forcing parameters on the geostrophic adjustment, in particular the vertical extension of the azimuthal vortex through the water column, we consider the kinetic energy density of the vortex integrated in depth and within a radius $r \approx 250$ km. An effective damping time scale, T_z^{eff}, is then found through a least-square fit of the analytic solution of the vertical diffusion initial value problem to the evolution of the kinetic energy in the simulation. Comparing the effective damping time scale to the diffusion time scale, $T_z = {L_z}^2/\nu_z$, given by the model viscosity is then a measure of whether the vortex adjusts faster or slower than the predicted vertical diffusion time. The reason for the deviation is the overlay of two distinct adjustment processes (cf. Section 3.1.1). In particular, the effective adjustment timescale is mostly related to the mixed-layer depth, as discussed in the following section. For the control run the last phase of the adjustment is about four times slower than diffusion only (Table 2). Changing the surface parameters ΔT_s, R_r and v_{10} then leads to even slower adjustment with relative time scales between 5.17 and 6.52 (Table 2).

3.2.2. Mixed-layer depth

Geostrophic adjustment of the vortex. As introduced in the previous section, the third phase of the geostrophic adjustment process can be characterized by the evolution of the kinetic energy of the excited azimuthal vortex underneath the wind forcing. By comparing the decay to the analytic solution of the vertical diffusion initial value problem we derived an effective damping time scale relative to the diffusion time scale given by the model viscosity, $T_z = {L_z}^2/\nu_z$ (Table 2). We find that deeper mixed layers generally lead to smaller relative effective damping time scales (Table 2). In particular, mixed layers shallower than $H_m = 500$ m lead to a slower damping and deeper mixed layers lead to a faster damping than predicted by the solution to the vertical diffusion initial value problem.

During this stage of the geostrophic adjustment there are two distinct processes leading to an approach of the geostrophic equilibrium (Section 3.1.1). The vertical diffusion of the azimuthal velocity leads to a deceleration above the depth of the vortex and an acceleration below. However, the bottom-intensified pressure anomaly drives a radially outward current which feeds back into the azimuthal component via the Coriolis effect and decelerates the vortex throughout the whole water column. The latter effect is aligned with the diffusion above the depth of the vortex and counteracts it below. As the vertical extent of the azimuthal vortex after the end of the forcing is similar to mixed-layer depth (Fig. 7) the diffusion is accelerated in simulations with shallower mixed layers and decelerated in simulations with deep mixed layers.

Generation and propagation of waves. Deeper mixed layers are generally associated to weaker stratification and thus to smaller amplitudes as well as reduced radial group velocities (Fig. 7a–f). Correspondingly, we observe waves propagating with reduced radial group velocities, here shown for the simulation with $H_m = 500$ m (Fig. 8). The forcing frequency, and thus the radial length scale, remain unchanged as the predicted group velocities approximately describe the propagation of the wave packets (gray lines in Fig. 8). As a consequence of the slower group velocities the wave packets with different vertical mode structure or slightly different frequency

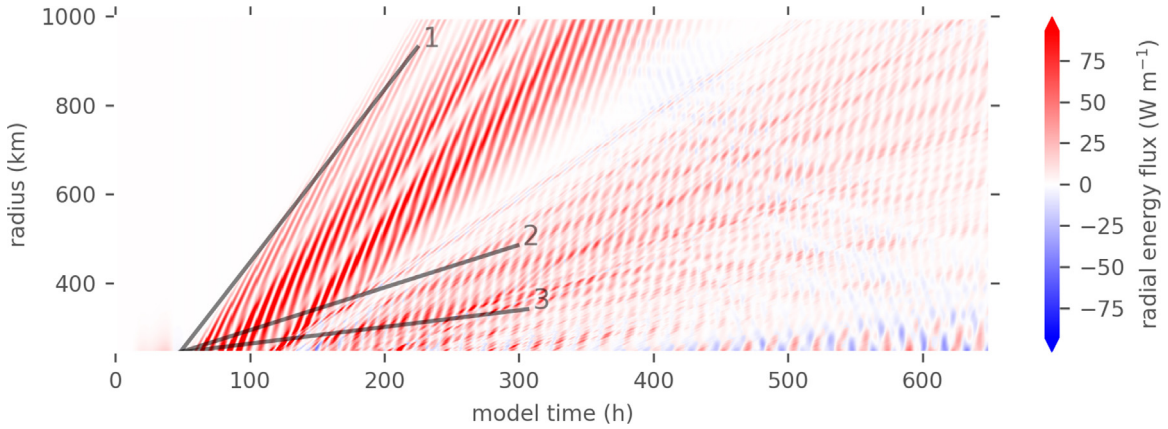

Fig. 8. Same as Fig. 4 but with $H_m = 500$ m. The radiated wave packets are characterized by weaker stratification and thus smaller group velocities. The associated energy fluxes are an order of magnitude smaller. Consequently the wave packets separate over shorter time scales. Due to the decreased radial group velocity a superposition of higher mode internal gravity waves occurs. Predicted group velocities from the vertical mode decomposition are shown as black overlays with indicated mode number. The radial wave number is assumed to be $k_r = \pi/R_r$.

separate at smaller radii and pass through the radius $r = 250$ km as separate wave packets. Moreover, continually generated higher mode wave packets at later times superimpose when the radial extent of the packets is larger than the radial distance between two successively generated wave packets (Fig. 8).

Naturally, zero stratification does not allow for the generation of internal gravity waves (Fig. 7g). Instead, the inertial oscillation is maintained over a longer time as it does not damp out by wave generation.

3.3. Energetics

3.3.1. Energetics of the control run

The energetics of the model reflect the above-described adjustment processes. The wind work is equal to the integral of the product of the wind shear stress exerted on the surface with the surface velocity itself. In the control simulation, it is approximately $\Phi_{\text{wind}} \approx 401$ TJ (Table 4). This corresponds to the predicted order of magnitude (Eq. (24)). The mechanical energy stored in the vortex below the forcing region by the end of control run is approximately $E_v \approx 40$ TJ. As discussed in Section 3.1.1, this energy depends on the vertical extent of the vortex at the time it is observed. Its magnitude by the end of the simulation time represents the state of adjustment and diffusion rather than the terminal value. The measured mechanical energy is an order of magnitude higher than predicted (Eq. (31)) but also subject to further dissipation. The total energy radiated as internal gravity waves in the control run is approximately $\Phi_{\text{IW}} \approx 60$ GJ. That result corresponds to the predicted order of magnitude (Eq. (27)) and is controlled by the excited angular frequency ω, the radial wave number k_r and the magnitude of the radial velocity A_u. Based on these results and the energy balance (Eq. (23)), the residual dissipation is about $D \approx 361$ TJ, or equivalently $D/\Phi_{\text{wind}} \approx 90\,\%$ of the wind energy input.

The energy transferred to internal gravity waves being only about 0.02% is several orders of magnitude smaller than reported previously. In similar studies using forcing with comparable structure but translating in the horizontal in 3-dimensional models found that a fraction of $\sim$25% is transferred to internal gravity waves (Price, 1983; Niwa and Hibiya, 1997). However, both formulations implement the wind forcing with a bulk formulation driving a surface slab rather than being treated as a surface friction. Here we do not assume a profile of vertical momentum transport associated to the wind. The resulting stress profile leads to highest values of dissipation close to the surface which is consistent with high energy losses in the mixed layer. The modeled wind power is comparable to the literature but the transport of momentum through the mixed layer may be less efficient when being mostly driven by horizontal friction.

Typical findings in observations and general circulation models range between 9% and 30% (e.g. D'Asaro et al., 1995; Alford et al., 2012; Rimac et al., 2016). Elevated values are particularly associated with the wake of hurricanes, i.e. strong storms (Price, 1983; Gill, 1984; D'Asaro et al., 1995). This study excludes effects based on the lateral movement of the storm, 3-dimensional instabilities and surface heat fluxes. This includes strong drivers of vertical motion like heat driven mixed-layer convection, mixed region collapse or turbulent motion in general. We therefore interpret that these processes may be essential for the efficient generation of internal gravity waves below storms.

3.3.2. The wind amplitude, radial length scale and forcing time scale

Forcing with a twice as long wind pulse ($\Delta T_s = 4$ days) leads to a wind work of $\Phi_{\text{wind}} \approx 911$ TJ (Table 3). Compared to the control run with $\Phi_{\text{wind}} = 401$ TJ, this increase corresponds to the longer forcing time. However, the out-of phase excitation of the inertial oscillation (cf. Section 3.2.1) halves the energy radiated as internal gravity waves compared to the control run, so that $\Phi_{\text{IW}} \approx 33$ GJ. Instead, a significantly larger portion is imparted into the vortex. The increase of the corresponding energy relative to the wind work, E_v/Φ_{wind}, from 10% in the control run to 17% is not associated to the stage of the geostrophic adjustment, i.e. to the vertical diffusion

Table 3
Energetics of model runs with the same mixed-layer depth H_m but double the wind speed v_{10}, double the critical radius of the Rankine vortex wind profile R_r or double the duration of the pulse from the control run. The dissipation D is the residual of all other terms (Eq. (23)). The first line is the control run with reference parameters $H_m = 50$ m, $R_r = 50$ km and $v_{10} = 30\ m\,s^{-1}$. The energies are measured at time $t = 40$ days.

H_m (m)	Φ_{wind} (TJ)	E_v/Φ_{wind} (%)	Φ_{IW}/Φ_{wind} (%)	D/Φ_{wind} (%)	Varied parameter
50	401	10	−0.015	−90	Control run
50	911	17	−0.004	−83	$\Delta T_s = 4$ days
50	1417	8	−0.02	−92	$R_r = 100$ km
50	5666	9	−0.025	−91	$v_{10} = 60\ m\,s^{-1}$

of the vortex, but to a correspondingly raised azimuthal velocity.

Increasing the critical radius of the Rankine vortex from that in the control run by a factor 2, so that $R_r = 100$ km, leads to a larger area on which the wind stress acts. Correspondingly, the wind work is increased to $\Phi_{wind} \approx 1417$ TJ (Table 3). The proportion of energy radiated as internal gravity waves relative to the wind work is only slightly increased (from 0.015% to 0.02%). Thus the length scale of the forcing has little influence on the excitation mechanisms for internal gravity waves which is consistent with the observation of very similar structures of the far field (cf. Section 3.2.1).

Here we recall that the surface velocity scales with the wind stress, which scales with the square of the wind velocity (Eqs. (10) and (24)). Hence, the wind power which is the product of the wind stress and the surface velocity, scales with the fourth power of the wind velocity. Doubling the wind speed therefore leads to significantly larger wind work. In simulations with $v_{10} = 60\ m\,s^{-1}$ the measured work is $\Phi_{wind} \approx 5666$ TJ, an increase by a factor of approximately 14 from the control run. The excited inertial oscillation has a larger amplitude and therefore takes a longer time to damp out. Even though the internal gravity waves do not change in structure (cf. Section 3.2.1) the radiated energy fluxes are larger by a factor 24, radiating an energy $\Phi_{IW} \approx 1438$ GJ (Table 3). Thus the radiated energy is not proportional to the wind work at increased wind speeds.

3.3.3. The role of the mixed-layer depth

It is observed that with increasing mixed-layer depth (and consequently decreasing maximum stratification), the energy transferred to the system decreases from 410 TJ at $H_m = 25$ m to 345 TJ in the run with $H_m = 3000$ m (Table (4)). At the same time, higher azimuthal vorticities (Eq. (1)) are observed. We interpret that a deeper mixed layer allows for a faster spin-up of the center vortex and the associated vertical velocity due to the reduced buoyancy. However, the increased positive radial velocity acts as a negative feedback on the azimuthal velocity via the Coriolis effect. Consequently, the azimuthal velocities are generally smaller and less energy is transferred through the ocean surface (Eq. (24)).

The mechanical energy stored in the vortex at the end of the model run ($t = 40$ days) is observed to decrease from $E_v = 46$ TJ (at $H_m = 25$ m) to $E_v = 11$ TJ (at $H_m = 3000$ m) (Table 4). However, this value depends on the state of the geostrophic adjustment as described above. A deeper mixed layer and a correspondingly reduced stratification below the mixed-layer base is associated with increased azimuthal vorticity or equivalently larger radial and vertical velocities. Hence, the vertical advection of the azimuthal velocity is stronger for deeper mixed layers and the vortex expands in depth on shorter time scales (Fig. 7). Consequently, the vertical extent of the center vortex at the end of the model run depends on the mixed-layer depth of the run. Thus, the mechanical energy stored in the center vortex at a fixed model time, e.g. $t = 40$ days, does not represent the energy the vortex will contain in the geostrophic equilibrium.

A reduced stratification has a positive feedback on the vertical velocities and thus on the inertial pumping amplitude as described above. However, we find that the total energy radiated reduces from $\Phi_{IW} = 64$ GJ in simulations with $H_m = 25$ m to $\Phi_{IW} = 12$ GJ in simulations with $H_m = 1000$ m. This decrease is associated with the decreased stratification as the mixed-layer depth increases. Naturally there is no generation of internal gravity waves in the zero stratification environment (cf. Table 4 and Fig. 7g).

Dissipation is implemented using a Laplacian diffusion operator (Eq. (4)). Therefore, it depends solely on the internal shear stresses. These are largest close to the surface where the wind stress imparts a strong shear. Therefore, most of the dissipation is

Table 4
Energetics of model runs with different H_m. The dissipation D is the residual of all other terms (Eq. (23)). Values in parenthesis are relative to the wind work in the second column. The last row indicates a run with zero stratification throughout the water column.

H_m (m)	Φ_{wind} (TJ)	E_v (TJ)	(E_v/Φ_{wind}) (%)	Φ_{IW} (GJ)	(Φ_{IW}/Φ_{wind}) (%)	D (TJ)	(D/Φ_{wind}) (%)
25	410	46	(11)	−64	(−0.016)	−364	(−89)
50	401	40	(10)	−60	(−0.015)	−361	(−90)
100	387	32	(8)	−51	(−0.013)	−355	(−92)
200	371	23	(6)	−37	(−0.01)	−347	(−94)
500	355	15	(4)	−21	(−0.006)	−339	(−96)
1000	348	12	(4)	−12	(−0.004)	−336	(−96)
3000	345	11	(3)	0		−334	(−97)

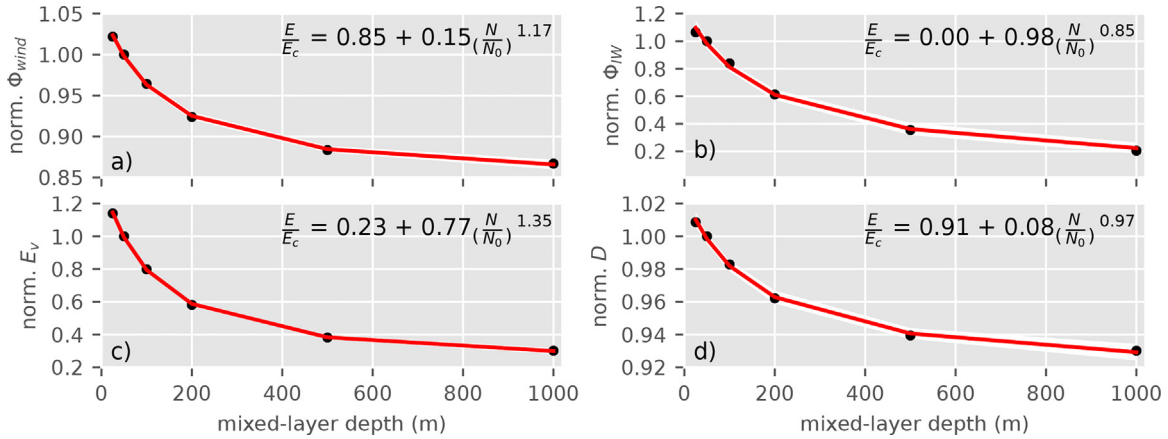

Fig. 9. Energy input (a), energy radiated as internal waves (b), energy transferred to the vortex (c), and energy dissipated (d) normalized with the corresponding value of the control run as function of mixed-layer depth. The energy dissipated is calculated as the residual of the energy balance (Eq. (23)). Scaling laws from non-linear least square fits following Eq. (33) are indicated. White shadings depict the 95% confidence intervals of the fits. For a list of all fit parameters see Table 5.

associated with shallow depth ($z \geq -60$ m) and depends little upon the mixed-layer depth. The absolute value of the dissipated energy for all simulations decreases moderately from $D = 364$ TJ to $D = 334$ TJ as the mixed-layer depth increases (Table 4). Note that this value depends, like the energy stored in the center vortex, on the state of adjustment and increases with time. This increase may be larger for shallower mixed-layer depths.

In order to quantify the scaling of the different components of the energy balance (Φ_{wind}, E_{v}, Φ_{IW}, and D) with the stratification at the mixed-layer depth, an asymptotic fit to the energies was found assuming the form

$$\frac{E}{E_c} = A + B\left(\frac{N(H_{\text{m}})}{N_0}\right)^C. \tag{33}$$

Here, E and E_c represent any of the above named energies and its value in the control run, respectively. The stratification is normalized with its reference value $N_0 = 10^{-2}$ rad/s (cf. Eq. (12) and Table 1). The parameters A, B and C are obtained by performing a non-linear least-squares fit. In such a scenario C directly determines the scaling behavior with respect to the maximum buoyancy frequency of the water column $N(H_{\text{m}})$. While the parameter A represents the asymptotic behavior associated to zero stratification, B is the scale of variation of the respective energy relative to the control run. Note that the fit of the radiated energy, Φ_{IW}, is forced through $A \equiv 0$.

We find that the wind work, Φ_{wind}, varies by approximately (15 ± 1) % with an exponent of 1.17 ± 0.22 (Fig. 9a). It is thus largely independent of the stratification with a moderate variability attributed to a Coriolis feedback mechanism described in Section 3.3.3. Even though the fit suggests a super-linear scaling, the confidence interval includes a linear relationship. In the case of the radiated energy, Φ_{IW}, the offset A is set to zero and Φ_{IW} must depend fully on the stratification (Fig. 9b). It shows a sub-linear scaling with an exponent of 0.85 ± 0.10. The non-linear fit of the energy stored in the vortex E_{v} suggests a variability of approximately (77 ± 4) % but is also subject to both further geostrophic adjustment and dissipation for shallower mixed layers as discussed in Sections 3.2.2 and 3.3.3 (Fig. 9c). Thus, the two effects, the reduced gravity wave radiation and the faster geostrophic adjustment (cf. Table 2), superimpose and the fit is difficult to interpret. Finally, the dissipation, **D**, has a variability of about (8 ± 1) % with an exponent of 0.97 ± 0.33 (Fig. 9d). Since the evolution of the center vortex after the simulation end may lead to more dissipated energy for shallower mixed layers the variability may be overestimated here. The fraction of dissipated energy is thus mostly independent of the stratification. All fit results are summarized in Table 5.

Table 5
Parameter results and base values from scaling fits (Eq. (33)). The last column corresponds to the zero stratification run. Errors are given by 95% confidence intervals from the non-linear fit. The fit of the radiated energy, Φ_{IW}, is simplified by setting $A \equiv 0$.

	E_c (TJ)	A (1)	B (1)	C (1)
Φ_{wind}	401.45	0.85 ± 0.02	0.15 ± 0.01	1.17 ± 0.22
Φ_{IW}	0.06	0	0.98 ± 0.04	0.85 ± 0.10
E_{v}	40.34	0.23 ± 0.04	0.77 ± 0.04	1.35 ± 0.14
D	361.04	0.91 ± 0.02	0.08 ± 0.01	0.97 ± 0.33

4. Summary and conclusion

We examined the generation of internal gravity waves by a stationary cyclonic wind stress pulse in a non-linear, axisymmetric and Boussinesq model. The wind pulse with a duration of $\Delta T_s = 2$ days is characterized by the Rankine vortex structure with a critical radius $R_r = 50$ km, a maximum wind speed of $v_{10} = 30$ m/s. Stratification profiles with decreasing buoyancy frequency with depth, $N(z) = s/(z_0 - z)$, following Gill (1984) are used. The mixed-layer depth varies between $H_m = 50$ m and $H_m = 1000$ m.

In general the evolution of the flow can be considered in three overlapping phases. During the linear increase of the wind velocity from zero to its maximum at time $t = 12$ h and the subsequent period of constant wind, the ocean surface is accelerated in the azimuthal and consequently in the radially outward direction. A radial flow and a corresponding return flow in the interior evolves immediately. The second phase, occurring after approximately one inertial period is characterized by the oscillation of the radial motion with the inertial frequency and the associated vertical velocity – the inertial pumping. Low vertical mode internal gravity waves are excited by the corresponding vertical motion through the stratified water column. Additionally, the oscillation of a bottom-intensified pressure anomaly dipole associated to the excited vortex excites upward propagating higher mode waves. The inertial oscillation damps out as internal gravity wave packets are radiated radially outward and the vortex reaches an approximate geostrophic balance. The third adjustment phase starts right after the end of the wind forcing at $t = 48$ h. It is characterized by the diffusion of the vortex in the vertical and the adjustment of the bottom-intensified pressure dipole until it eventually reaches the geostrophic equilibrium. The equilibrium was not observed within the model run time of 40 days.

The wave number-frequency spectrum at the mixed-layer base reveals that the generated wave packets follow distinct dispersion relations similar to the analytically derived relation associated to the vertical normal modes. The structure of the generated waves is controlled by the forcing time scale as well as the stratification rather than the horizontal length scale in the forcing.

Around 90% of the energy incurred by the wind is dissipated close to the surface. This is due to the vertical momentum transfer through internal stresses only. Around 10% of the wind energy stays within the vortex and only about 0.01% of the energy is radiated from the vortex as internal gravity waves. Increasing the mixed-layer depth while keeping the assumed stratification profile in the deep ocean constant (i.e. N_0, z_0 and $z_{ref} \equiv$ const ., cf. Eq. (12) and Table 1) decreases the maximum stratification occurring at the base of the mixed layer. This mimics the mixing of the ocean above the mixed-layer depth without influencing the stratification below. Consequently an increased mixed-layer depth leads to a reduction of the energy radiated as internal gravity waves and stored in the vortex. However, the latter is subject to further adjustment towards the geostrophic equilibrium at the end of the model time.

The energy radiated as internal gravity waves relative to the wind power is several orders of magnitude lower than 10–30%, as typically observed in the ocean and general circulation models (D'Asaro et al., 1995; Alford et al., 2012; Rimac et al., 2016). We interpret that other processes that drive vertical motion like surface heat fluxes, turbulent motion, mixed region collapse and storm translation are essential for significant energy extraction by internal gravity waves to occur. In particular the wake behind a laterally translating storm was reported to contain elevated internal gravity wave energy levels with transfer rates ~25% in similar but 3-dimensional setups (Price, 1983; Niwa and Hibiya, 1997).

The wind driven inertial pumping is a well known source of internal gravity waves that has been frequently investigated (e.g. Gill, 1984; Moehlis and Smith, 1999; Tsai et al., 2008). However, the commonly observed excitation mechanism differs from the mechanisms considered here, specifically by the depth of the inertial pumping. While the inertial oscillations in the present simulations spread through the whole water column, observations of moving storms suggest the forcing of near-surface oscillations by the wind and a subsequent excitation of vertically propagating near-inertial gravity waves (e.g. Price et al., 1991; Dohan and Davis, 2011; Forryan et al., 2015). To the authors' knowledge there has been no description of the excitation of higher mode waves through the inertial oscillation of a bottom pressure anomaly to date. This has potential impact on the parametrization of unresolved internal gravity waves in general circulation models, their corresponding energy distribution, and eventual ocean mixing. However, the low energy transfer rates observed in this study are posing questions on the importance of the mechanisms described here which require further investigation to be answered.

Acknowledgements

This study was supported by the Deutsche Forschungsgemeinschaft (DFG) through the International Research Training Group "Processes and impacts of climate change in the North Atlantic Ocean and the Canadian Arctic" (IRTG 1904 ArcTrain). Moreover, this work is a contribution to the Collaborative Research Centre TRR 181 "Energy Transfer in Atmosphere and Ocean", funded by the German Research Foundation. P.G. Myers gratefully acknowledges the financial and logistic support of grants from the Natural Sciences and Engineering Research Council (NSERC) of Canada. These include a Discovery Grant (rgpin 227438-09) and an International Create (ArcTrain – 432295). B.R. Sutherland is funded through the Natural Sciences and Engineering Research Council (NSERC) Discovery Grant program.

Appendix A. A 4th order wave number cutoff filter

The relation between the azimuthal vorticity ζ and the stream function ψ in the radius-depth plane is given by Eq. (6). In particular,

$$\Delta_r \psi - \frac{\psi}{r^2} = -\zeta \tag{A.1}$$

with the Laplace operator in radial coordinates $\Delta_r = r^{-1}\partial/\partial_r(r\partial/\partial_r) + \partial^2/\partial_z^2$. Note that this is the Poisson equation in cylindrical coordinates. The no-normal flow conditions on the top and the bottom boundary of the domain imply that the stream function is zero at both boundaries. Moreover, the stream function is zero at the inner boundary, i.e. at $r = 0$, due to the symmetry. Hence, the above equation can be solved using a Fourier-sine-transform in the vertical and a Bessel-transform of order $n = 1$ (Eq. (8)) in the radial direction. However, strong gradients in the azimuthal vorticity may induce ringing in the discretized radial transform on a bounded interval. To suppress noise, a 4th order exponential cutoff filter, adapted from LaCasce (1996), is introduced.

Consider the azimuthal vorticity ζ and its Fourier–Bessel transform

$$\mathcal{Z}(k_r, k_z) = \mathcal{F}_{\mathrm{SFB}}(\zeta(r, z)) = \int_{-H}^{0}\int_{0}^{\infty} \sin(k_z z)\mathrm{r}J_1(k_r r)\zeta(r, z)\mathrm{d}r\,\mathrm{d}z, \tag{A.2}$$

in which J_1 is the Bessel function of the first kind of order $n = 1$, H is the depth of the domain, k_r is the radial and k_z the vertical wave number. Due to the bounded domain and the no-normal flow boundary conditions, the vertical wave number is discretized so that $k_z = l\pi/H$ with $l \in \mathbb{N}$. It is worth mentioning that the sine expansion in depth represents an orthonormal set of functions but is not equal to the vertical mode expansion in the present stratification. With $\Psi = \mathcal{F}_{\mathrm{SFB}}(\psi)$, Eq. (6) is solved by $\Psi = \mathcal{Z}/({k_r}^2 + {k_z}^2)$ and the corresponding inverse transform. In the code, these are discretized transforms so that both the radial and the vertical wave number are discrete and have a maximum wave number corresponding to the Nyquist wave number – analogous to the Nyquist frequency. Suppose, a discrete transformed vorticity $\mathcal{Z}_n$ and maximal mode number n_{Ny} of the Fourier–Bessel series. The filter function is set up so that

$$\tilde{\mathcal{Z}}_n = \begin{cases} \mathcal{Z}_n, & 0 < n \le n_{\mathrm{co}} \\ \mathcal{Z}_n \cdot \exp(-36.8(n - n_{\mathrm{co}})^4(n_{\mathrm{Ny}} - n_{\mathrm{co}})^{-4}), & n_{\mathrm{co}} < n \le n_{\mathrm{Ny}} \end{cases} \tag{A.3}$$

is the filtered coefficient of the azimuthal vorticity in the Fourier–Bessel space. The mode number n_{co} is equivalent to a radial cut-off length scale equal to 10 km. The factor -36.8 $(\ln(10^{-16}))$ is determined by the double precision machine accuracy and the exponent, 4, is chosen so that the filter is smooth enough and does not cause ringing itself. This filter acts like a low pass for radial structures larger than the cut-off length scale.

Appendix B. The vertical mode decomposition in axisymmetric coordinates

Based on the linearized and frictionless equations of motion in azimuthal symmetry the stream function ψ can be separated according to

$$\psi(r, z, t) = A_\psi \hat{\psi}(z) J_1(k_r r)\exp(i\omega t) \tag{B.1}$$

where A_ψ is the amplitude, $\hat{\psi}$ is the vertical component, J_1 the Bessel function of the first kind of order 1 and ω is the angular frequency of the internal gravity wave. Note that $\hat{\psi}$ has the unit m. The ordinary differential equation for the vertical structure, i.e. $\hat{\psi}$, reads then

$$0 = \frac{d^2}{\mathrm{d}z^2}\hat{\psi} + {k_r}^2\frac{N^2(z) - \omega^2}{\omega^2 - f^2}\hat{\psi}. \tag{B.2}$$

As usual, k_r is the radial wave number and f is the Coriolis frequency. The buoyancy frequency is given by (compare Eq. (12))

$$N(z) = \begin{cases} 0 & 0 > z > -H_{\mathrm{m}} \\ \frac{s}{z_0 - z} & -H_{\mathrm{m}} \ge z > -H \end{cases} \tag{B.3}$$

Within the mixed layer we can define the mixed-layer vertical wave number ${q_{\mathrm{m}}}^2 = {k_r}^2\omega^2/(\omega^2 - f^2)$ and solve Eq. (B.2) for the mixed-layer stream function $\hat{\psi}_{\mathrm{m}}$, obeying the rigid-lid condition. Ultimately we get

$$\hat{\psi}_{\mathrm{m}}(z) = A\sinh(q_{\mathrm{m}} z). \tag{B.4}$$

Note that Eq. (B.4) can be approximated as a linear function for small $q_{\mathrm{m}}z$. To find the solution within the stratified region we define the scaled vertical coordinate ζ with $s\,d\zeta = N\,dz$ so that $\hat{\psi}_{\mathrm{s}}(\zeta) = \hat{\psi}(z)$ with

$$0 = \frac{d}{d\zeta}\hat{\psi}_{\mathrm{s}} + \frac{d^2}{d\zeta^2}\hat{\psi}_{\mathrm{s}} + {k_r}^2 s^2\frac{1 - \frac{\omega^2}{N^2}}{\omega^2 - f^2}\hat{\psi}_{\mathrm{s}}. \tag{B.5}$$

We solve Eq. (B.5) by approximating $N^2 \gg \omega^2$ so that

$$\hat{\psi}_{\mathrm{s}}(\zeta) = B\exp\left(-\frac{\zeta}{2}\right)\sin(q_{\mathrm{s}}\zeta) \quad \text{with} \quad {q_{\mathrm{s}}}^2 = \frac{{k_r}^2 s^2}{\omega^2 - f^2}. \tag{B.6}$$

Matching the two solutions at the mixed-layer depth and requiring continuity gives the scaling condition

$$\frac{A}{B} = \frac{\exp\left(-\frac{\zeta_{\mathrm{m}}}{2}\right)\sin(q_{\mathrm{s}}\zeta_{\mathrm{m}})}{\sinh(-q_{\mathrm{m}}H_{\mathrm{m}})}, \tag{B.7}$$

and the discretization condition

$$\frac{N_m}{s}\left[q_s \cot(q_s \zeta_m) - \frac{1}{2}\right] = q_m \coth(-q_m H_m), \tag{B.8}$$

where ζ_m and N_m are the scaled vertical coordinate and the mixed-layer stratification at the mixed-layer depth, respectively. The relation between the vertical wave numbers is obtained requiring the radial wave number to be equal within and below the mixed layer. In particular

$$q_s{}^2 = \frac{q_m{}^2 s^2}{\omega^2} - \frac{1}{4}. \tag{B.9}$$

Eq. (B.8) can then be solved numerically. Moreover we require that the radial group velocities in the mixed layer and the stratified region are the same. The latter conditions lead then to the dispersion relation

$$\omega^2 = f^2\left(1 - \frac{k_r{}^2}{q_m{}^2}\right)^{-2}. \tag{B.10}$$

Comparing the definition of the mixed-layer vertical wave number, q_m, and Eq. (B.10) then gives the long wave condition

$$q_m{}^2 \gg k_r{}^2. \tag{B.11}$$

References

Alford, M.H., 2001. Internal swell generation: the spatial distribution of energy flux from the wind to mixed layer near-inertial motions. J. Phys. Oceanogr. 31, 2359–2368. https://doi.org/10.1175/1520-0485(2001)031<2359:ISGTSD>2.0.CO;2.

Alford, M.H., Cronin, M.F., Klymak, J.M., 2012. Annual cycle and depth penetration of wind-generated near-inertial internal waves at Ocean Station Papa in the Northeast Pacific. J. Phys. Oceanogr. 42, 889–909. https://doi.org/10.1175/JPO-D-11-092.1.

Alford, M.H., Whitmont, M., 2007. Seasonal and spatial variability of near-inertial kinetic energy from historical moored velocity records. J. Phys. Oceanogr. 37, 2022–2037. https://doi.org/10.1175/JPO3106.1.

Bars, M.L., Lecoanet, D., Perrard, S., Ribeiro, A., Rodet, L., Aurnou, J.M., Gal, P.L., 2015. Experimental study of internal wave generation by convection in water. Fluid Dyn. Res. 47, 045502. https://doi.org/10.1088/0169-5983/47/4/045502.

Bulatov, V.V., Vladimirov, Y.V., 2018. Far fields of internal gravity waves from a nonstationary source. Oceanology 58, 796–801.

Danioux, E., Klein, P., Rivière, P., 2008. Propagation of wind energy into the deep ocean through a fully turbulent mesoscale eddy field. J. Phys. Oceanogr. 38, 2224–2241. https://doi.org/10.1175/2008JPO3821.1.

D'Asaro, E.A., Eriksen, C., Levine, M., Niiler, P., Paulson, C., Meurs, P.V., 1995. Upper-ocean inertial currents forced by a strong storm. Part I: Data and comparisons with linear theory. J. Phys. Oceanogr. 25, 2909–2936.

Dippe, T., Zhai, X., Greatbatch, R.J., Rath, W., 2015. Interannual variability of wind power input to near-inertial motions in the North Atlantic. Ocean Dyn. 65, 859–875. https://doi.org/10.1007/s10236-015-0834-x.

Dohan, K., Davis, R.E., 2011. Mixing in the transition layer during two storm events. J. Phys. Oceanogr. 41, 42–66. https://doi.org/10.1175/2010JPO4253.1.

Duck, P.W., Foster, M.R., 2001. Spin-up of homogeneous and stratified fluids. Annu. Rev. Fluid Mech. 33, 231–263.

Ferrari, R., Wunsch, C., 2009. Ocean circulation kinetic energy: reservoirs, sources, and sinks. Annu. Rev. Fluid Mech. 41, 253–282. https://doi.org/10.1146/annurev.fluid.40.111406.102139.

Forryan, A., Naveira Garabato, A.C., Polzin, K.L., Waterman, S., 2015. Rapid injection of near-inertial shear into the stratified upper ocean at an Antarctic Circumpolar Current front. Geophys. Res. Lett. 3431–3441. https://doi.org/10.1002/2015GL063494.

Fu, L., 1981. Observations and models of inertial waves in the deep ocean. Rev. Geophys. 19, 141–170. https://doi.org/10.1029/RG019i001p00141.

Furuichi, N., Hibiya, T., Niwa, Y., 2008. Model-predicted distribution of wind-induced internal wave energy in the world's oceans. J. Geophys. Res.: Oceans 113, C09034. https://doi.org/10.1029/2008JC004768.

Gill, A.E., 1984. On the behavior of internal waves in the wakes of storms. J. Phys. Oceanogr. 14, 1129–1151. https://doi.org/10.1175/1520-0485(1984)014<1129:OTBOIW>2.0.CO;2.

Holdsworth, A.M., Sutherland, B.R., 2013. Influence of lock aspect ratio upon the evolution of an axisymmetric intrusion. J. Fluid Mech. 735, 1–11. https://doi.org/10.1017/jfm.2013.517.

Jensen, T.G., 1998. Open boundary conditions in stratified ocean models. J. Mar. Syst. 16 (3–4), 297–322.

Kang, D., Fringer, O., 2010. On the calculation of available potential energy in internal wave fields. J. Phys. Oceanogr. 40, 2539–2545. https://doi.org/10.1175/2010JPO4497.1.

LaCasce, J.H., 1996. Baroclinic Vortices Over a Sloping Bottom (Ph.D. thesis). MIT/WHOI.

Leaman, K.D., 1976. Observations on the vertical polarization and energy flux of near-inertial waves. J. Phys. Oceanogr. 6, 894–908. https://doi.org/10.1175/1520-0485(1976)006<0894:OOTVPA>2.0.CO;2.

Leaman, K.D., Sanford, T.B., 1975. Vertical energy propagation of inertial waves: a vector spectral analysis of velocity profiles. J. Geophys. Res. 80, 1975–1978.

Lecoanet, D., Le Bars, M., Burns, K.J., Vasil, G.M., Brown, B.P., Quataert, E., Oishi, J.S., 2015. Numerical simulations of internal wave generation by convection in water. Phys. Rev. E – Stat. Nonlinear Soft Matter Phys. 91, 1–10. https://doi.org/10.1103/PhysRevE.91.063016.

McMillan, J.M., Sutherland, B.R., 2010. The lifecycle of axisymmetric internal solitary waves. Nonlinear Process. Geophys. 17, 443–453. https://doi.org/10.5194/npg-17-443-2010.

Moehlis, J., Smith, S.G.L., 1999. Radiation of mixed layer near-inertial oscillations into the ocean interior. J. Phys. Oceanogr. 31, 15. https://doi.org/10.1175/1520-0485(2001)031<1550:ROMLNI>2.0.CO;2.

Moulin, F.Y., Flór, J.-B., 2004. On the spin-up by a rotating disk in a rotating stratified fluid. J. Fluid Mech. 516, 155–180. https://doi.org/10.1017/S0022112004000655.

Nagasawa, M., Niwa, Y., Hibiya, T., 2000. Spatial and Temporal Distribution of the Wind-Induced Internal Wave Energy Available for Deep Water Mixing in the North Pacific. https://doi.org/10.1029/2000JC900019.

Niwa, Y., Hibiya, T., 1997. Nonlinear processes of energy transfer from traveling hurricanes to the deep ocean internal wave field. J. Geophys. Res. 102, 12464–12477.

Price, J.F., 1983. Internal wave wake of a moving storm. Part I. Scales, energy budget and observations. J. Phys. Oceanogr. 13, 949–965. https://doi.org/10.1175/1520-0485(1983)013<0949:IWWOAM>2.0.CO;2.

Price, J.F., Sanford, T.B., Forristall, G.Z., 1991. Ocean Response to a Hurricane. Part II: Data Tabulations and Numerical Modeling. Technical Report. Woods Hole Oceanographic Institution, Woods Hole.

Rimac, A., Storch, J.S.V., Eden, C., 2016. The total energy flux leaving the ocean's mixed layer. J. Phys. Oceanogr. 16. https://doi.org/10.1175/JPO-D-15-0115.1.
Sanford, T.B., Price, J.F., Girton, J.B., 2011. Upper-ocean response to Hurricane Frances (2004) observed by profiling EM-APEX floats*. J. Phys. Oceanogr. 41, 1041–1056. https://doi.org/10.1175/2010JPO4313.1.
Schubert, W.H., Hack, J.J., Silva Dias, P.L., Fulton, S.R., 1980. Geostrophic adjustment in an axisymmetric vortex. J. Atmos. Sci. 37, 1464–1484. https://doi.org/10.1175/1520-0469(1980)037<1464:GAIAAV>2.0.CO;2.
Tsai, Y., Chern, C.-S., Wang, J., Box, P.O., 2008. The upper ocean response to a moving typhoon. J. Oceanogr. 64, 115–130.
Wunsch, C., Ferrari, R., 2004. Vertical mixing, energy, and the general circulation of the oceans. Annu. Rev. Fluid Mech. 36, 281–314. https://doi.org/10.1146/annurev.fluid.36.050802.122121.